

Variation of the magnetic ordering in GdT_2Zn_{20} ($T=Fe, Ru, Os, Co, Rh$ and Ir) and its correlation with the electronic structure of isostructural YT_2Zn_{20}

Shuang Jia (贾爽),^{1,2} Ni Ni (倪霓),^{1,2} G. D. Samolyuk,¹ A. Safa-Sefat,¹ K. Dennis,¹ Hyunjin Ko,^{1,3} G. J. Miller,^{1,3} S. L. Bud'ko,^{1,2} and P. C. Canfield^{1,2}

¹United States Department of Energy, Ames Laboratory, Iowa State University, Ames, Iowa 50011, USA

²Department of Physics and Astronomy, Iowa State University, Ames, Iowa 50011, USA

³Department of Chemistry, Iowa State University, Ames, Iowa 50011, USA

(Received 14 December 2007; revised manuscript received 8 February 2008; published 10 March 2008)

Magnetization, resistivity, and specific heat measurements were performed on solution-grown single crystals of six GdT_2Zn_{20} ($T=Fe, Ru, Os, Co, Rh,$ and Ir) compounds, as well as on their Y analogs. For the Gd compounds, the Fe column members manifest a ferromagnetic (FM) ground state (with an enhanced Curie temperature T_C for $T=Fe$ and Ru), whereas the Co column members manifest an antiferromagnetic (AFM) ground state. Thermodynamic measurements on YT_2Zn_{20} revealed that the enhanced T_C for $GdFe_2Zn_{20}$ and $GdRu_2Zn_{20}$ can be understood within the framework of Heisenberg moments embedded in a nearly ferromagnetic Fermi liquid. Furthermore, electronic structure calculations indicate that this significant enhancement is due to a large transition metal partial density of states at the Fermi level that places these compounds close to the Stoner FM criterion. The change from FM to AFM ordering (between the Fe and Co column materials) is associated with the filling of electronic states with two additional electrons/f.u. The degree of this sensitivity is addressed by the studies of the pseudoternary compounds $Gd(Fe_xCo_{1-x})_2Zn_{20}$ and $Y(Fe_xCo_{1-x})_2Zn_{20}$, which clearly reveal the effect of $3d$ -band filling on their magnetic properties.

DOI: [10.1103/PhysRevB.77.104408](https://doi.org/10.1103/PhysRevB.77.104408)

PACS number(s): 75.50.Cc, 75.50.Ee, 75.30.Cr, 71.20.Lp

I. INTRODUCTION

The magnetism of rare earth intermetallics, determined by the interaction between $4f$ local moments and conduction electrons, especially the d -band conduction electrons of transition metals, has been of interest to physicists for the past several decades.^{1,2} Recently, studies of the dilute and rare earth bearing intermetallic compounds, RT_2Zn_{20} (R =rare earth and T =transition metal in $Fe, Co,$ or neighboring columns), revealed varied exotic magnetic properties.³⁻⁵ Although they contain less than 5 at. % rare earth ions which, although dilute, fully occupy a unique crystallographic site, these compounds allow for the study of local and hybridizing moment magnetism in a regime that approaches the single ion limit while preserving periodicity. Previous studies of these compounds have indicated that they can serve as model systems for a variety of physical phenomena ranging from a nearly ferromagnetic Fermi liquid (NFFL) (YFe_2Zn_{20} and $LuFe_2Zn_{20}$),³ to a greatly enhanced ferromagnetic (FM) order in $GdFe_2Zn_{20}$,^{3,5} all the way to heavy fermion ground states in YbT_2Zn_{20} ($T=Fe, Ru, Os, Co, Rh,$ and Ir).⁴

The RT_2Zn_{20} series of compounds was discovered in 1997 by Nasch *et al.*⁶ These compounds assume the isostructural cubic $CeCr_2Al_{20}$ structure,⁷⁻⁹ in which the R and T ions each occupy their own single unique crystallographic site with cubic and trigonal point symmetries, respectively, and the Zn ions occupy three unique crystallographic sites. The coordination polyhedra for R and T are fully comprised of Zn , meaning that there are no R - R , T - T , or R - T nearest neighbors and the shortest R - R spacing is ~ 6 Å. The nearest-neighbor and next-nearest-neighbor shells of the R are all Zn , forming an all Zn Frank-Kasper polyhedron around the site and isolating it.⁶ RT_2Zn_{20} compounds had been found to form for

$T=Fe, Ru, Co,$ and Rh , but no thermodynamic or transport property measurements were reported. As part of this study, we have extended the range of known RT_2Zn_{20} compounds to $T=Os$ and Ir series.

In rare earth bearing intermetallic compounds, $R=Gd$ members give the clearest indication of the strength and sign of the magnetic interaction, without any complications associated with crystalline electric field splitting of the Hund's rule ground state multiplet. In order to better understand the RT_2Zn_{20} series of compounds, in this paper we examine the thermodynamic and transport properties of six GdT_2Zn_{20} ($T=Fe, Ru, Os, Co, Rh,$ and Ir) compounds as well as their $R=Y$ analogs. We found FM transitions in the iron column members (with enhanced T_C values for $T=Fe$ and Ru) and low-temperature antiferromagnetic (AFM) transitions in the cobalt column members. Consistent with these results, we also found enhanced paramagnetism in the $T=Fe$ and Ru of YT_2Zn_{20} analogs. For $GdFe_2Zn_{20}$ and $GdRu_2Zn_{20}$, magnetization measurements under hydrostatic pressure indicated that their enhanced FM transitions are not primarily associated with a steric effect. A model of Heisenberg moments embedded in a NFFL can be proposed as a way to understand the enhanced FM transitions. Band structure calculations were employed to explain that the remarkable differences in magnetic ordering for different transition metal members are a result of different d -band fillings. In order to test this further, a series of pseudoternary compounds $Y(Fe_xCo_{1-x})_2Zn_{20}$ and $Gd(Fe_xCo_{1-x})_2Zn_{20}$ was made, which was characterized and found to manifest a clear, systematic, and comprehensible evolution from a normal to a nearly FM metal and from an AFM state to a high-temperature FM state, respectively, associated with a change of the d -band filling as x varies from 0 to 1.

II. EXPERIMENTAL METHODS AND CALCULATION DETAILS

Single crystals of RT_2Zn_{20} ($R=Gd$ and Y ; $T=Fe, Co, Ru, Rh, Os,$ and Ir) were grown from a Zn-rich self-flux.^{3,10} The initial molar ratio of starting elements ($R:T:Zn$) were 2:4:96 ($T=Fe$ and Co), 1:2:97 ($T=Ru$ and Rh), 1:0.5:98.5 ($T=Os$), and 0.75:1.5:97.75 ($T=Ir$). High purity constituent elements were placed in alumina crucibles and sealed in silica tubes under approximately 0.33 atm of high purity Ar. Then, the ampoules were heated to 1000 °C ($T=Fe$ and Co), 1150 °C ($T=Ru$), 1100 °C ($T=Rh$), and 1150 °C ($T=Os$ and Ir), held at these temperatures for 3 h, and cooled down to 600, 850, 700, and 750 °C, respectively, at which point the remaining liquid was decanted. The cooling rates were 5 °C/h ($T=Fe, Co, Ru,$ and Rh), 4 °C/h ($T=Os$), and 2.5 °C/h ($T=Ir$). Growths such as these often had only two to three nucleation sites per crucible and yielded crystals with typical dimensions of $7 \times 7 \times 7$ mm³ or larger except for the Os compounds, which were significantly smaller (1–2 mm on one side). The residual flux and/or oxide slag on the crystal surfaces was removed by using diluted acid (0.5 vol % HCl in H₂O for $T=Fe$ and Co , and 1 vol % acetic acid in H₂O for $T=Ru, Rh, Os,$ and Ir). The samples were characterized by room temperature powder x-ray diffraction measurements using Cu $K\alpha$ radiation with Si ($a=5.43088$ Å) as an internal standard. The lattice constants were obtained by using the Rietveld refinement program RIETICA.

Subsequent single-crystal x-ray analyses were made by using a STOE image plate diffractometer with Mo $K\alpha$ radiation, which used the supplied STOE software.¹¹ The data were adjusted for Lorentz and polarization effects, and a numerical absorption correction was done. The structural solutions were refined by full-matrix least-squares refinement using the Bruker SHELXTL 6.1 software package.¹² The atomic disorder in the crystals was checked by refining site occupancies.

The magnetization measurements under hydrostatic pressure were performed in a piston-cylinder, clamp-type pressure cell made of a nonmagnetic Ni-Co alloy, MP35N, in Quantum Design superconducting quantum interface device (SQUID) magnetometers. Pressure was generated in a Teflon capsule filled with a 50:50 mixture of *n*-pentane and mineral oil. The pressure dependent superconducting transition temperature of 6N purity Pb was employed to determine the pressure at low temperatures.¹³ The pressure cell design allows for the routine establishment of pressures in excess of 8 kbar at low temperatures.¹⁴

Measurements of the electrical resistivity were made by using a standard ac four-probe technique. The samples were cut into bars, which typically had lengths of 2–3 mm, parallel to the crystallographic [110] direction. ac electrical resistivity measurements were taken on these bars with $f=16$ Hz and $I=0.5$ – 0.3 mA in Quantum Design physical property measurement systems: PPMS-14 and PPMS-9 instruments ($T=1.85$ – 310 K). Temperature dependent specific heat measurements were also performed by using the heat capacity option of these Quantum Design instruments. dc magnetization was measured in Quantum Design SQUID

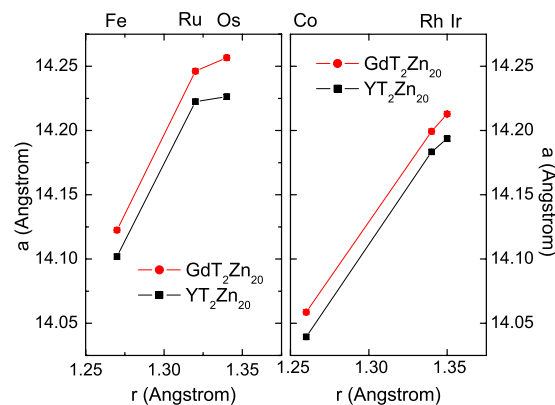


FIG. 1. (Color online) The lattice constants (a) of GdT_2Zn_{20} and YT_2Zn_{20} versus the Goldschmidt radius (r) of the transition metal with coordination number 12 (Ref. 22)

magnetometers in an applied field ≤ 55 kOe or 70 kOe and in a temperature range of 1.85–375 K.

In general, when making magnetization measurements on FM samples, some attention must be paid to the effects of demagnetizing fields.¹⁵ However, this correction is small in the case of GdT_2Zn_{20} because of the diluted nature of the magnetic moments. Considering that the magnetization is mainly from eight Gd^{3+} ions per unit cell, one estimates the maximum demagnetizing field as follows:

$$D_m(Max) = 4\pi \frac{8(7\mu_B)}{(14 \text{ \AA})^3} = 2380 \text{ Oe.} \quad (1)$$

Experimentally, in the measurements of magnetization isotherms near the T_C , the demagnetizing field can introduce an error for platelike samples. To avoid this error, rodlike samples were measured with an applied magnetic field along their long axis. This minimized the demagnetizing factor and, therefore, the demagnetizing field.

The electronic structure was calculated by using the atomic sphere approximation tight binding linear muffin-tin orbital method,^{16,17} which used the experimental values of the lattice parameters and atomic positions from this work. The exchange-correlation term was calculated within both the local-spin-density approximation, which was parametrized according to von Barth–Hedin,¹⁸ and the generalized gradient approximation with the Perdew–Burke–Ernzerhof functional.¹⁹ A mesh of 16 \vec{k} points in the irreducible part of the Brillouin zone was used. The 4*f* electrons of the Gd atoms were treated as polarized core states. Despite its apparent simplicity, this approach reproduces the electronic and magnetic properties of rare earths, which is in good agreement with experiment.^{20,21} In order to reproduce the AFM ordering in $GdCo_2Zn_{20}$, the magnetic moments of two Gd atoms in the unit cell were aligned in opposing directions.

III. RESULTS AND ANALYSIS

A. Structure refinements

Figure 1 shows that the lattice parameters, determined by the refinement of powder x-ray diffraction, increase as the

TABLE I. Atomic coordinates and refined site occupancies for $\text{GdFe}_2\text{Zn}_{20}$ and $\text{GdRu}_2\text{Zn}_{20}$; each of the unique crystallographic sites were refined individually. The total number of reflections and the number of refined parameters are 7887 and 8336, and 17 and 17 for $\text{GdFe}_2\text{Zn}_{20}$ and $\text{GdRu}_2\text{Zn}_{20}$, respectively.

Atom	$Fd\bar{3}m$	Occupancy	x	y	z	U_{eq} (\AA^2)
$\text{GdFe}_2\text{Zn}_{20}$, $a=14.1232(16)$ \AA , $R_1=0.0286$						
Gd	$8a$	1	0.125	0.125	0.125	0.006(1)
Fe	$16b$	1	0.5	0.5	0.5	0.006(1)
Zn1	$96g$	1	0.0587(1)	0.0587(1)	0.3266(1)	0.014(1)
Zn2	$48f$	1	0.4893(1)	0.125	0.125	0.010(1)
Zn3	$16c$	1	0	0	0	0.021(1)
$\text{GdRu}_2\text{Zn}_{20}$, $a=14.2564(16)$ \AA , $R_1=0.0335$						
Gd	$8a$	1	0.125	0.125	0.125	0.008(1)
Ru	$16b$	1	0.5	0.5	0.5	0.007(1)
Zn1	$96g$	1	0.0589(1)	0.0589(1)	0.3260(1)	0.015(1)
Zn2	$48f$	1	0.4888(1)	0.125	0.125	0.011(1)
Zn3	$16c$	1	0	0	0	0.023(1)

transition metal varies from $3d$ to $5d$ for both $\text{GdT}_2\text{Zn}_{20}$ and $\text{YT}_2\text{Zn}_{20}$. The error bars, smaller than the symbols in the plot, were estimated from the standard variation of multiple measurement results on one batch of samples. In addition to the refinement of powder x-ray diffraction, the crystallographic atomic site occupancies and positions were refined using single-crystal x-ray diffraction data on the crystals of $\text{GdFe}_2\text{Zn}_{20}$ and $\text{GdRu}_2\text{Zn}_{20}$. As shown in Table I, both compounds were found to be fully stoichiometric within 3σ . The atomic site positions are very close to the isostructural compounds reported before.⁶ It should be noted though that the similar atomic number values for Zn and Fe made it difficult to completely resolve possible mixed site occupancies.

B. $\text{GdT}_2\text{Zn}_{20}$ ($T=\text{Fe, Co, Ru, Rh, Os, and Ir}$)

Before discussing each of the $\text{GdT}_2\text{Zn}_{20}$ compounds separately, an overview of their temperature and field dependent magnetization serves as a useful point of orientation. In Fig. 2, the temperature dependent magnetization (M) divided by the applied field (H) reveals the primary difference between the Fe column members of this family and the Co column members. For $T=\text{Fe, Ru, and Os}$, there is an apparent FM ordering (with remarkably high and moderately high values of T_C for $T=\text{Fe}$ and Ru , respectively), whereas for $T=\text{Co, Rh, and Ir}$, there is an apparent low-temperature AFM ordering.

The nature of the ordering is further confirmed by the low-temperature magnetization isotherms presented in Fig. 3. It should be noted that for each of the six $\text{GdT}_2\text{Zn}_{20}$ compounds, the 1.85 K magnetization isotherms, which were measured with the applied field along $[100]$, $[110]$, and $[111]$ crystallographic directions, were found to be isotropic to within less than 5%. This magnetic isotropy is not unexpected in Gd-based intermetallics, in which magnetism is mainly due to the pure spin contribution of the $4f$ shell of Gd^{3+} . For $T=\text{Fe, Ru, and Os}$, magnetization is representative

of a FM-ordered state with a rapid rise and saturation of the ordered moment in a field of the order of the estimated demagnetizing field (with the magnetic domain wall pinning being low in these single crystalline samples). For $T=\text{Co, Rh, and Ir}$, the field dependent magnetization data are consistent with AFM-ordered states that can be field stabilized to fully saturated states in large enough applied magnetic fields. This fully saturated state is observed for $\text{GdCo}_2\text{Zn}_{20}$, which is associated with a spin-flop transition near $H=31$ kOe, whereas the maximum magnetic field in the equipment used (55 kOe) could not saturate the magnetic moment of the $\text{GdRh}_2\text{Zn}_{20}$ and $\text{GdIr}_2\text{Zn}_{20}$ samples. The measured saturated moments for $T=\text{Fe, Ru, Os, and Co}$ samples are clustered around the Hund's rule ground state value of $\text{Gd}^{3+}(7\mu_B)$.

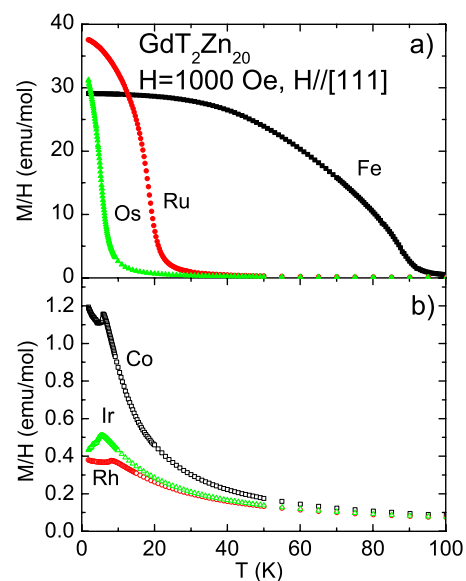


FIG. 2. (Color online) Temperature dependent magnetization of $\text{GdT}_2\text{Zn}_{20}$ divided by the applied field $H=1000$ Oe.

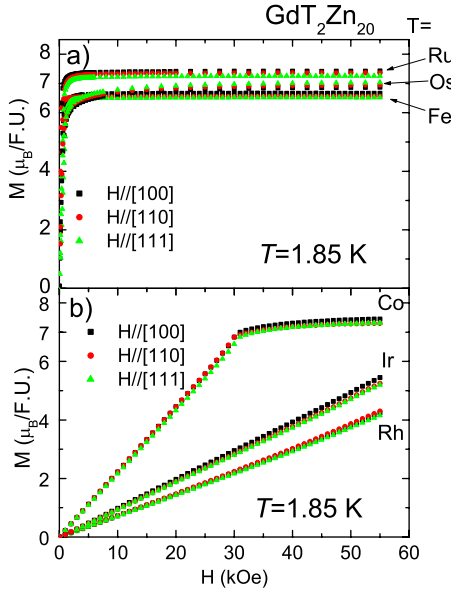


FIG. 3. (Color online) Field dependent magnetization of GdT_2Zn_{20} at 1.85 K for an applied magnetic field along all three principal directions: [100], [110], and [111].

Figure 4 presents temperature dependent H/M data for the six Gd-based compounds. For this low magnetic field, H/M approximately equals the inverse susceptibility $[1/\chi(T)]$ in the paramagnetic state. Except for $GdFe_2Zn_{20}$, the data sets of $1/\chi(T)$ of these compounds are linear and parallel to each other over the whole temperature range of the paramagnetic state, manifesting a Curie–Weiss (CW) behavior, $\chi(T) = C/(T - \theta_C)$, where C is the Curie constant and θ_C is the paramagnetic Curie temperature. Similar C values are extracted from the nearly parallel lines that give similar effective moments ($\mu_{\text{eff}} \approx 8\mu_B$) that are close to the value of Hund’s rule ground state of $Gd^{3+}(7.94\mu_B)$, without any apparent contribution from local moments that could be associated with the transition metal (see Table II below). This is consistent with the low-temperature saturated moments that are close to the theoretical value of $\mu_{\text{sat}} = 7\mu_B$ (Fig. 3). In contrast, $1/\chi(T)$ of $GdFe_2Zn_{20}$ obeys a simple CW law only above ~ 200 K and evidently deviates from it at lower tem-

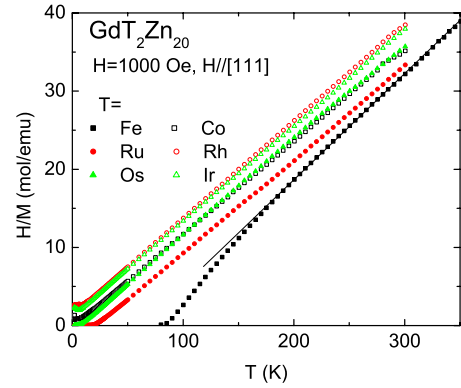


FIG. 4. (Color online) Applied field ($H=1000$ Oe) divided by the magnetizations of GdT_2Zn_{20} as a function of temperature. The solid line represents the high-temperature CW fit for $GdFe_2Zn_{20}$.

peratures (see discussion below). Nevertheless, its high-temperature CW behavior yields μ_{eff} close to the other values. The sign of the θ_C values is consistent with their magnetic ordering type, except for $GdCo_2Zn_{20}$, which manifests an AFM order but with a positive, albeit small, θ_C (Table II). This anomalous θ_C value for $GdCo_2Zn_{20}$, compared to the values for $T=\text{Rh}$ and Ir members, leads to a much larger susceptibility near the Néel temperature T_N (Fig. 2).

$GdFe_2Zn_{20}$ has the most conspicuously anomalous behavior.³ Figure 5 presents a blowup of the low field M/H data as well as the results of measurements of temperature dependent specific heat (C_p) and electrical resistivity (ρ) in zero applied magnetic field. The specific heat data manifest a clear anomaly at $T_C = 85 \pm 1$ K [inset of Fig. 5(b)]. The resistivity data, although collected from a sample from a different batch, show a clear break in slope (or maximum in $d\rho/dT$) at $T_C = 84 \pm 2$ K. The determination of the ordering temperature from magnetization data requires a more detailed analysis. Figure 6 presents a plot of M^2 versus H/M (an Arrott plot²³) from data collected on the same batch of sample used for C_p in the vicinity of T_C . The isotherm that most closely goes linearly through the origin is the one closest to T_C , giving a value of 88 K.³ All of these measurements are consistent with a transition temperature near 86 K. It

TABLE II. Lattice constant a (± 0.002 Å), residual resistivity ratio $\text{RRR} = R(300 \text{ K})/R(2 \text{ K})$, paramagnetic Curie temperature θ_C , effective moment μ_{eff} [from the CW fit of $\chi(T)$ from 100 to 300 K, except for $GdFe_2Zn_{20}$; see text for details], magnetic ordering temperature, T_C or T_N , and saturated moment μ_{sat} at 55 kOe along the [111] direction on GdT_2Zn_{20} compounds ($T=\text{Fe}, \text{Ru}, \text{Os}, \text{Co}, \text{Rh}, \text{and Ir}$).

T	Fe	Ru	Os	Co	Rh	Ir
a (Å)	14.1226	14.2462	14.2567	14.0587	14.1994	14.2129
RRR	8.1	7.6	5	12.8	12.8	15.7
θ_C (K)	46	23	3	3	-10	-8
μ_{eff}, μ_B	7.9	8.2	8.1	8.2	8.0	8.1
T_C (K)	86	20	4.2			
T_N (K)				5.7	7.7	4.1, 2.8 ^a
μ_{sat}, μ_B	6.5	7.25	6.9	7.3		

^aTwo magnetic transitions were found.

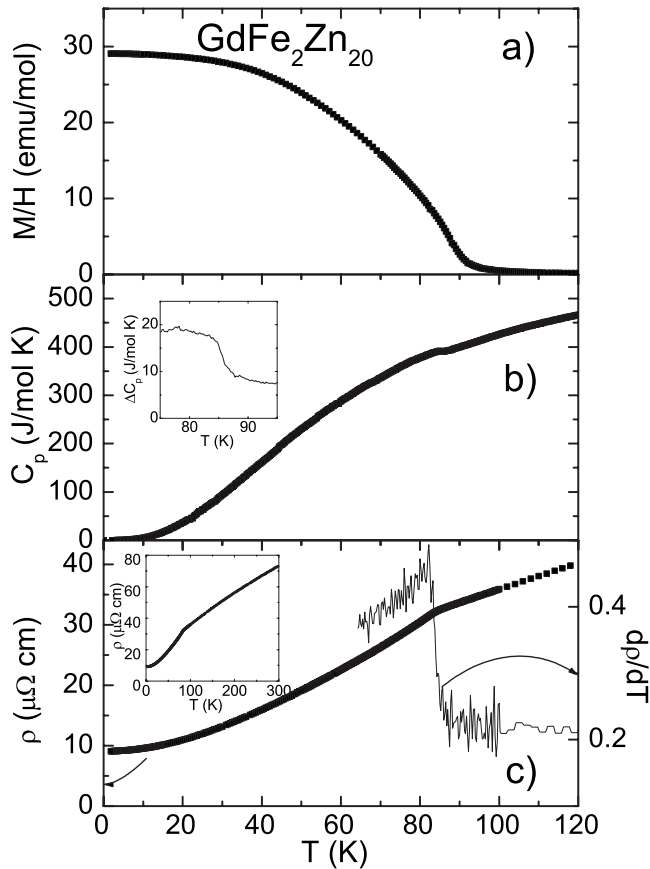


FIG. 5. (a) Temperature dependent magnetization (M) of $\text{GdFe}_2\text{Zn}_{20}$ divided by the applied field ($H=1000$ Oe), (b) specific heat (C_p), and (c) resistivity (ρ) and its derivative with respect to temperature ($d\rho/dT$). Inset in (b): The magnetic part of specific data estimated as $\Delta C_p = C_p(\text{GdFe}_2\text{Zn}_{20}) - C_p(\text{LuFe}_2\text{Zn}_{20})$ near T_C . Inset in (c): ρ over the whole temperature range of 2–300 K.

should be noted that T_C values for different batches of samples can vary by as much as ± 3 K, even though the single-crystal x-ray diffraction measurements do not suggest evident crystallographic differences.

$\text{GdRu}_2\text{Zn}_{20}$ also manifests a relatively high FM ordering temperature. Figures 7(b) and 7(c) present temperature dependent specific heat and electrical resistivity measurements for $\text{GdRu}_2\text{Zn}_{20}$ in zero applied magnetic fields, both of which

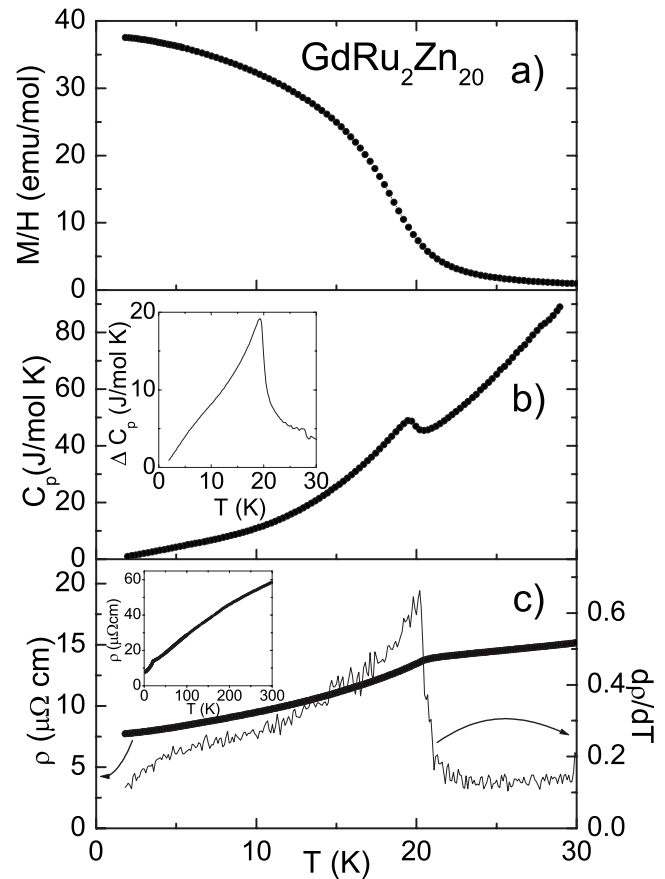


FIG. 7. (a) Temperature dependent M/H for $\text{GdRu}_2\text{Zn}_{20}$ ($H = 1000$ Oe), (b) C_p , and (c) ρ and $d\rho/dT$. Inset in (b): The magnetic part of specific data estimated as $\Delta C_p = C_p(\text{GdRu}_2\text{Zn}_{20}) - C_p(\text{LuRu}_2\text{Zn}_{20})$. Inset in (c): ρ over the whole temperature range.

show clear evidence of ordering with $T_C = 20 \pm 1$ K. Figure 8 shows that, similar to $\text{GdFe}_2\text{Zn}_{20}$, the T_C of $\text{GdRu}_2\text{Zn}_{20}$ can be inferred from an Arrott plot analysis. These measurements were performed on samples from the same batch, and the different methods for determining T_C agree to within ± 1 K.

$\text{GdOs}_2\text{Zn}_{20}$ appears to order ferromagnetically at a T_C value as low as the Néel temperatures found for the Co column members of the $\text{GdT}_2\text{Zn}_{20}$ family (see below). As shown in Figs. 9(b) and 9(c), the specific heat and resistivity

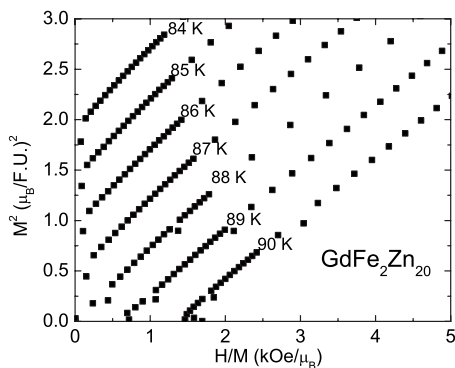


FIG. 6. Arrott plot of magnetic isotherms for $\text{GdFe}_2\text{Zn}_{20}$.

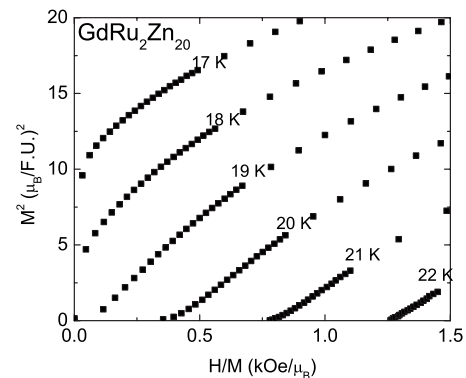


FIG. 8. Arrott plot of magnetic isotherms for $\text{GdRu}_2\text{Zn}_{20}$.

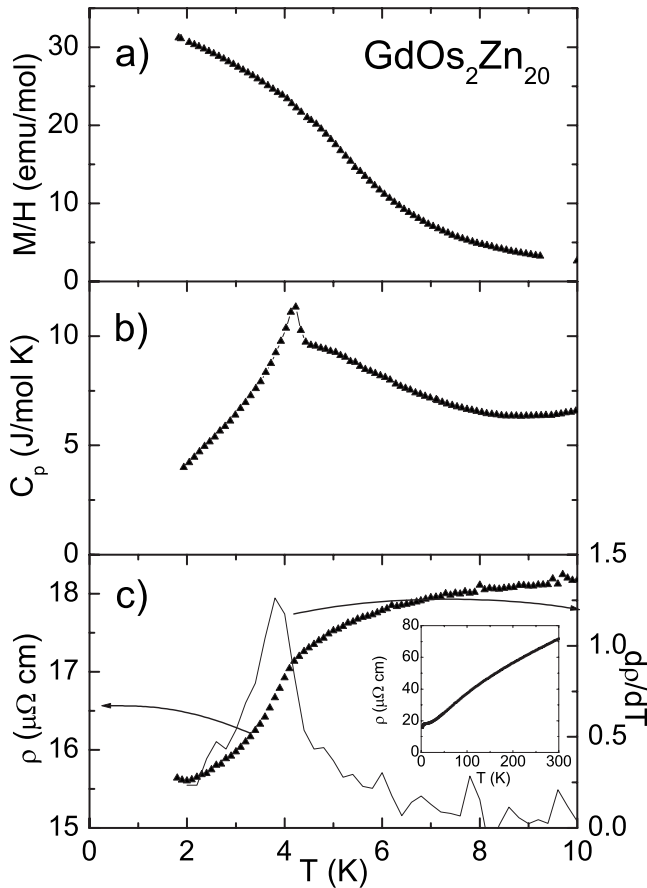


FIG. 9. (a) Temperature dependent M/H for $\text{GdOs}_2\text{Zn}_{20}$ ($H = 1000$ Oe), (b) C_p , and (c) ρ and $d\rho/dT$. Inset in (c): ρ over the whole temperature range.

data manifest features consistent with a magnetic phase transition near 4 K. However, the C_p data, with a broad shoulder above this temperature, do not manifest a standard λ type of feature and may indicate a distribution of T_C values or multiple transitions. The Arrott plot for $\text{GdOs}_2\text{Zn}_{20}$, although having nonlinear isothermal curves, is also consistent with a FM transition between 4 and 4.5 K (Fig. 10). Such a nonlinear feature in the isothermal curves is also found in Refs. 24

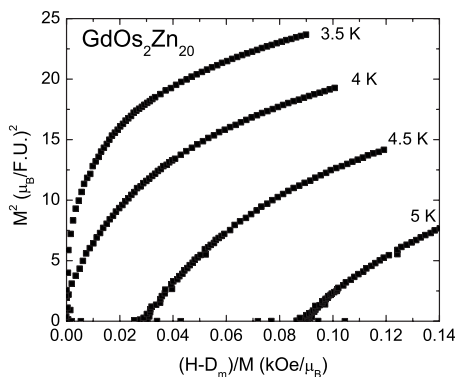


FIG. 10. Arrott plot of magnetic isotherms for $\text{GdOs}_2\text{Zn}_{20}$. The demagnetizing field D_m cannot be ignored for this low T_C and was estimated from the geometric factor of the sample ($D \sim 0.03$).

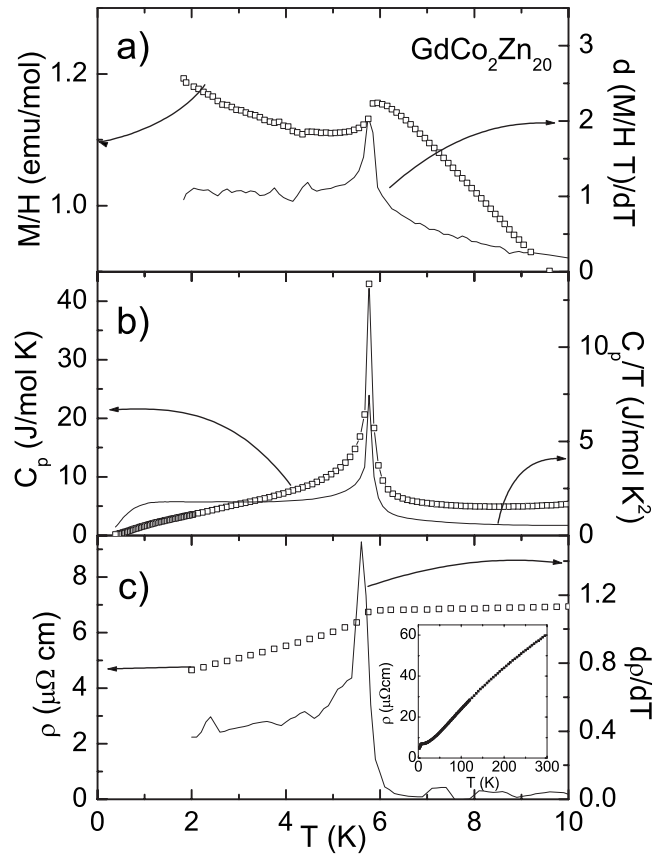


FIG. 11. (a) Temperature dependent susceptibility (χ) and $d(\chi T)/dT$ of $\text{GdCo}_2\text{Zn}_{20}$, (b) C_p and C_p/T , and (c) ρ and $d\rho/dT$. Inset in (c): ρ over the whole temperature range.

and 25 and may be associated with the complex magnetic phenomena in the critical region rather than with a simple clearly defined Landau type second order phase transition.

In contrast to the Fe column compounds, the Co column compounds all appear to order antiferromagnetically with values of T_N between 4 and 7 K. Figures 11–13 present the low-temperature magnetic susceptibility, specific heat, and electrical resistivity data for $\text{GdCo}_2\text{Zn}_{20}$,³ $\text{GdRh}_2\text{Zn}_{20}$, and $\text{GdIr}_2\text{Zn}_{20}$, respectively. In addition to these data, $d[\chi(T)T]/dT$ (Ref. 26) and $d\rho/dT$ (Ref. 27) have been added to the susceptibility and resistivity plots, respectively. $\text{GdCo}_2\text{Zn}_{20}$ and $\text{GdRh}_2\text{Zn}_{20}$ manifest clear λ -type anomalies in their temperature dependent specific heat, with similar features appearing in their $d\rho/dT$ and $d[\chi(T)T]/dT$ data. From these thermodynamic and transport data, we infer T_N of 5.7 ± 0.1 K and 7.7 ± 0.1 K for $\text{GdCo}_2\text{Zn}_{20}$ and $\text{GdRh}_2\text{Zn}_{20}$, respectively. Below their T_N , the susceptibility shows a slight increase with decreasing temperature. However, the temperature dependent C_p and C_p/T data show no anomaly except for the one associated with T_N [Figs. 11(b) and 12(b)]. $\text{GdIr}_2\text{Zn}_{20}$ shows a somewhat broader feature at $T_N = 4.1 \pm 0.1$ K, and there may be a lower temperature transition near 3 K indicated in the magnetization data, although this is not clearly supported by corresponding features in either specific heat or resistivity data. A summary of the thermodynamic and transport measurements on the six $\text{GdT}_2\text{Zn}_{20}$ compounds is presented in Table II.

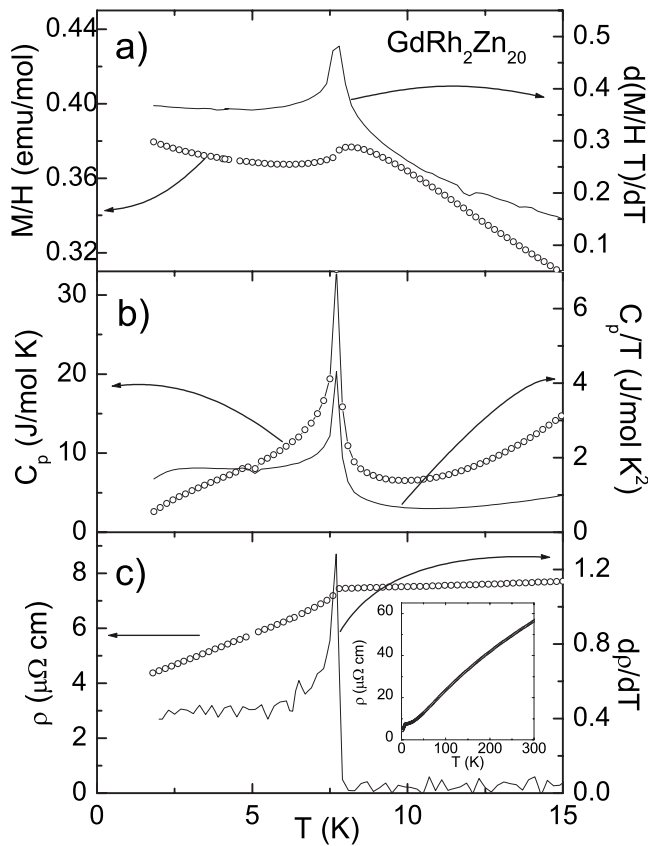


FIG. 12. (a) Temperature dependent χ and $d(\chi T)/dT$ of $\text{GdRh}_2\text{Zn}_{20}$, (b) C_p and C_p/T , and (c) ρ and $d\rho/dT$. Inset in (c): ρ over the whole temperature range.

A logical question that comes to mind when comparing T_C for the Fe column members with the lattice parameter data shown in Fig. 1 is whether the drop in T_C , as the transition metal moves down the column, is associated with a steric effect. This can be addressed experimentally by measuring the T_C under hydrostatic pressure. The temperature dependent low field magnetizations for $\text{GdFe}_2\text{Zn}_{20}$ and $\text{GdRu}_2\text{Zn}_{20}$ were measured under pressures up to 7 kbar. The pressure dependence of $T_{10\%}$, the temperature at which the magnetization equals 10% of the maximum low-temperature magnetization and which is used as a caliper of T_C , of each compound is plotted in Fig. 14. The fact that both compounds manifest decreases in T_C with increasing pressure indicates that the difference between $\text{GdFe}_2\text{Zn}_{20}$ and $\text{GdRu}_2\text{Zn}_{20}$ is not primarily a steric one. By approximating the bulk modulus of these compounds to be a generic 1 Mbar, one can estimate that $\text{GdRu}_2\text{Zn}_{20}$ under 10 kbar of hydrostatic pressure will have its lattice parameter reduced by 0.03 Å (25% of the difference between the lattice parameter of $\text{GdFe}_2\text{Zn}_{20}$ and $\text{GdCo}_2\text{Zn}_{20}$). If the cause of the T_C suppression was purely steric, such a change in lattice parameter should (at the very least) result in a dramatic increase in the T_C values of $\text{GdRu}_2\text{Zn}_{20}$ rather than the observed gradual decrease.

C. $\text{YT}_2\text{Zn}_{20}$ ($T=\text{Fe, Co, Ru, Rh, Os, and Ir}$)

In order to better understand the behavior of $\text{GdFe}_2\text{Zn}_{20}$ and $\text{GdRu}_2\text{Zn}_{20}$ with respect to the rest of the $\text{GdT}_2\text{Zn}_{20}$

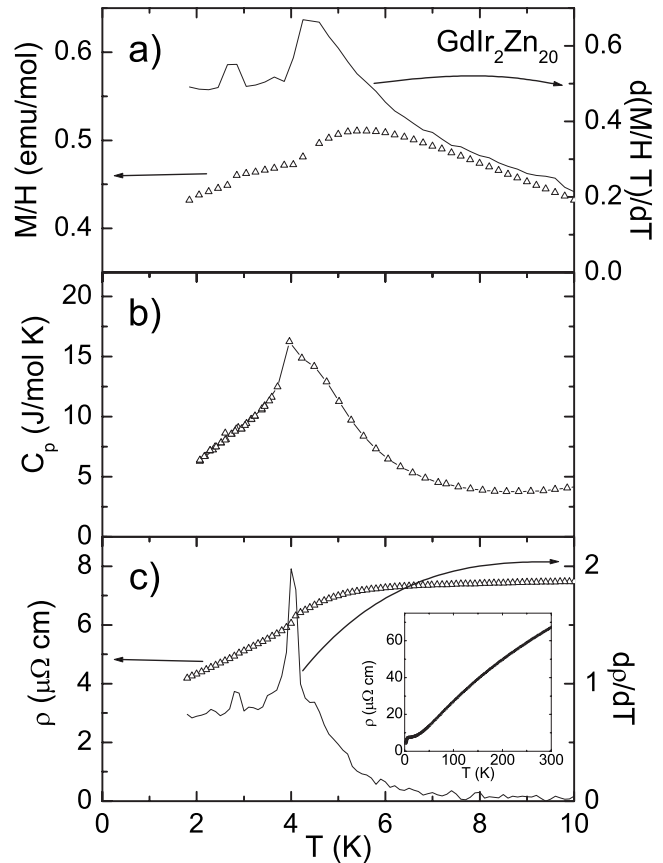


FIG. 13. (a) Temperature dependent χ and $d(\chi T)/dT$ of $\text{GdIr}_2\text{Zn}_{20}$, (b) C_p , and (c) ρ and $d\rho/dT$. Inset in (c): ρ over the whole temperature range.

compounds, it is useful to examine the properties of the non-magnetic analogs: the $\text{YT}_2\text{Zn}_{20}$ compounds. The temperature dependent magnetization data (divided by the applied field) and the low-temperature magnetization isotherms for these six compounds are presented in Figs. 15 and 16, respectively. $\text{YFe}_2\text{Zn}_{20}$ and $\text{YRu}_2\text{Zn}_{20}$ show great and intermediate enhancements of paramagnetic signals, respectively, whereas the rest of the materials manifest an ordinary and weak, either paramagnetic or diamagnetic, response that is expected of non-moment-bearing intermetallic compounds.

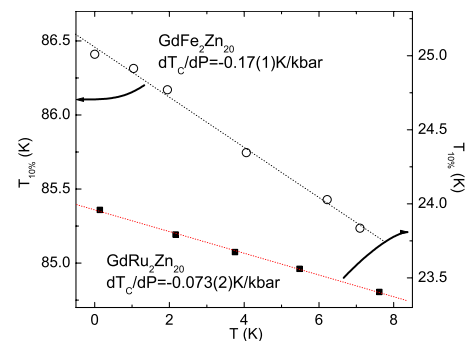


FIG. 14. (Color online) Pressure dependent $T_{10\%}$ (a caliper of T_C) of $\text{GdFe}_2\text{Zn}_{20}$ and $\text{GdRu}_2\text{Zn}_{20}$. The dash lines are the linear fits of the data.

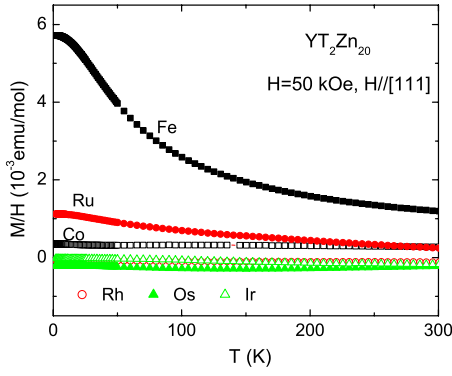


FIG. 15. (Color online) Temperature dependent magnetization of YT_2Zn_{20} under applied field $H=50$ kOe.

Measurements of the low-temperature specific heat (plotted as C_p/T versus T^2 in Fig. 17) also indicate a clear difference between YFe_2Zn_{20} , YRu_2Zn_{20} , and the other members of the YT_2Zn_{20} series: Enhanced values of the electronic specific heat are found for $T=Fe$ and Ru . As previously reported,³ YFe_2Zn_{20} can be considered as a compound that is close to the Stoner limit. The simplest way to see this is to recall that in this limit, whereas the Pauli paramagnetism is enhanced by a factor of $(1-Z)^{-1}$, the electronic specific heat is not.²⁸ This means that the term Z in the enhancement factor can then be inferred from the experimentally determined low-temperature values of γ_0 and χ_0 . In common units,

$$Z = 1 - 1.37 \times 10^{-2} \frac{\gamma_0(\text{J/mol K}^2)}{\chi_{0-dia}(\text{emu/mol})}, \quad (2)$$

where $\chi_{0-dia} = \chi_0$, with the core diamagnetism subtracted.

From the core diamagnetism values (-2.3×10^{-4} emu/mol for YFe_2Zn_{20} and YCo_2Zn_{20} , -2.5×10^{-4} emu/mol for YRu_2Zn_{20} and YRh_2Zn_{20} , and -2.9×10^{-4} emu/mol for YOs_2Zn_{20} and YIr_2Zn_{20}),²⁹ Z can be inferred to be 0.88 and 0.67 for YFe_2Zn_{20} and YRu_2Zn_{20} , respectively (Table III). For reference, this can be compared to $Z=0.83$ and 0.57 for elemental Pd and Pt, respectively (Table IV),³⁰ which are thought to be canonical examples of NFFL. These enhanced Z values indicate that YRu_2Zn_{20} and,

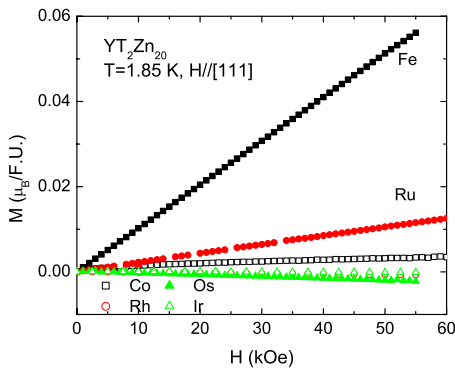


FIG. 16. (Color online) Field dependent magnetization of YT_2Zn_{20} at 1.85 K.

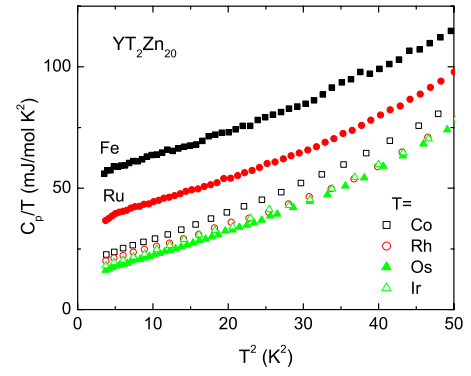


FIG. 17. (Color online) Low-temperature specific heat of YT_2Zn_{20} .

in particular, YFe_2Zn_{20} are extremely close to the Stoner limit ($Z=1$). In contrast, the Z values of the rest of the members are less than 0.5, which is comparable with the estimated value of the canonical example of the “normal metal” Cu , $Z=0.29$.³¹ It is worth noting that during the estimation of the Z values, the contribution from Landau diamagnetism is ignored. As it is inversely proportional to the square of the effective mass of the conduction electrons,³² the Landau diamagnetic contribution becomes more significant for those members that have smaller γ_0 values. Thus, based on the thermodynamic measurements, the Pauli susceptibility values, even after the core diamagnetism correction, are still underestimated. Due to this uncertainty, the Pauli susceptibility values after the core diamagnetism correction for YOs_2Zn_{20} and YRh_2Zn_{20} , albeit positive, are still less than the unenhanced values ($Z=0$) corresponding to their γ_0 .

D. Electronic structure

Band structure calculations, performed on the representative nonlocal moment members, YT_2Zn_{20} ($T=Fe, Co,$ and Ru), as well as on their local moment analogs, GdT_2Zn_{20} , can shed further light on their diverse magnetic properties. Figure 18 shows the result of the total and partial density of states (DOS) for each element for YFe_2Zn_{20} . At the Fermi level E_F , the total DOS manifests a sharp peak, leading to the relatively large DOS at the Fermi level [$N(E_F)$, see Table IV] and, therefore, to a large band contribution to the electronic specific heat, $\gamma_{band}=37$ mJ/mol K^2 . This result is consistent with the experimentally measured electronic specific heat γ_0 with a mass enhanced factor of $\lambda=0.43$ if one assumes $\gamma_0 = (1+\lambda)\gamma_{band}$. This mass enhanced factor, containing both electron-phonon and electron-electron contributions, is close to that for Pd ($\lambda \sim 0.5$) as well as for Ni_3Ga ($\lambda \sim 0.6$)³³. The peak-shape DOS at E_F is not unusual for the NFFL systems: Similar calculation results have been obtained for Pd,³⁴ YCo_2 ,³⁵ and Ni_3Ga (Ref. 33) by using similar techniques. The large peak at about -7 eV corresponds to totally filled d states of Zn atoms. Figure 18 also shows the significant contribution of the Zn atoms’ electronic states to the total DOS in the whole energy spectrum, whereas the Fe atoms’ electronic states are mostly localized in the vicinity of E_F , although they are dilute in this compound (1/10 of Zn). In

TABLE III. Lattice constant a (± 0.002 Å), low-temperature susceptibility χ_0 , the values after core diamagnetism correction χ_{0-dia} , linear coefficient of the specific heat γ_0 , Debye temperature θ_D , and the Stoner enhancement factor Z on YT_2Zn_{20} compounds ($T=Fe, Ru, Os, Co, Rh, \text{ and } Ir$).

T	Fe	Ru	Os	Co	Rh	Ir
a (Å)	14.1020	14.2226	14.2263	14.0395	14.1834	14.1937
χ_0^a	5.73	1.14	-0.256	0.212	-0.076	-0.034
χ_{0-dia}	5.96	1.39	0.034	0.442	0.174	0.256
γ_0^b	53	34	12.4	18.3	16.4	14.1
θ_D (K)	123	124	125	121	127	124
Z^c	0.88	0.67		0.43		0.24

^aTaken as $M(50 \text{ kOe}) - M(30 \text{ kOe}) / 20 \text{ kOe}$ in units of 10^{-3} emu/mol.

^bIn units of mJ/mol K².

^cEquation (2) is invalid for $T=Os$ and Rh ; see text.

order to estimate the enhancement factor Z , we used the partial $N(E_F)$ values for the transition metal and the results for exchange integrals I obtained by Janak in Ref. 36. The results, listed in Table IV, show that the theoretical Z value of 1.3 for YFe_2Zn_{20} is in between the values for elemental Pd ($Z=0.9$) and Fe ($Z=1.6$, before band splitting)—the canonical examples of nearly ferromagnet and “strong” ferromagnet systems. This result indicates that YFe_2Zn_{20} may indeed be even closer to the Stoner criterion than Pd. As we can see, the theoretical value is overestimated by $\pm 30\%$ compared to the experimental one. The total DOS at E_F mainly corresponds to the hybridization of the $3d$ band of Fe and the p band of Zn; the $4d$ band of Y, although hybridized with the other two, contributes significantly less (Fig. 18).

The dominant effect of the d -band filling on the magnetic properties of YT_2Zn_{20} manifests itself more clearly if one compares the electronic structure of the three YT_2Zn_{20} compounds: $T=Fe, Co, \text{ and } Ru$ (Fig. 19). The total and Co-partial DOSs of YCo_2Zn_{20} are similar to those of the YFe_2Zn_{20} analog, with the twice smaller Co-partial DOS at E_F being understood from the DOS of YFe_2Zn_{20} after shifting the Fermi energy 0.3 eV higher, which corresponds to the addi-

tion of two extra valence electrons/f.u. On the other hand, the electronic structure of YRu_2Zn_{20} has the same Fermi level position as YFe_2Zn_{20} because of the same valence electron filling. However, its total and Ru-partial DOSs are lower than those of YFe_2Zn_{20} . This difference is not unexpected since the $4d$ band is usually broader than the $3d$ band in the electronic structure of intermetallics. The calculated $N(E_F)$ for YCo_2Zn_{20} is one-half of the value for YFe_2Zn_{20} , whereas the value for YRu_2Zn_{20} is slightly larger for YCo_2Zn_{20} (Table IV).

The electronic structure calculation for the three GdT_2Zn_{20} analogs, based on the treatment of $4f$ electrons in core states, can also shed light on the effect of a submerging Gd^{3+} local moment in these electronic backgrounds (Y analogs). Our calculations demonstrate that in the ordered state, Gd and transition metals carry magnetic moments (see Table IV). Magnetic moments of Gd atoms are about $7.4\mu_B$ for the FM-ordered compounds and $7.3\mu_B$ for the AFM-ordered compound, which are significantly smaller compared to the result for elemental Gd,^{20,21} i.e., $7.6\mu_B$. The magnetic moment additional to Hund’s value ($7\mu_B$) comes from the polarization of Gd $6p$ and $5d$ states by magnetic $4f$ electrons.

TABLE IV. The calculated DOS in St/eV cell [$N(E_F)$, one cell has 2 f.u.], averaged DOS per atom [$N(E_F)/N_{atoms}$], partial DOS at transition metal atom [$N_T(E_F)$], exchange energy in eV for transition metal atom (I) (Ref. 36), calculated Stoner enhancement factor for transition metal atom [$Z_{cal}=N_T(E_F)I$], estimated Stoner enhancement factor (Z) by Eq. (2), and magnetic moment in μ_B for Gd and transition metal, T , in GdT_2Zn_{20} compounds.

Compound	$N(E_F)$	$N(E_F)/N_{atoms}$	$N_T(E_F)$	I	Z_{cal}	Z	Magnetic moment	
							Gd	T
Pt (elemental)	2.2	2.2	2.2			0.57		
Pd (elemental)	2.6	2.6	2.6	0.34	0.88	0.83		
Fe (elemental)	3.5	3.5	3.5	0.46	1.62			
YCo_2Zn_{20}	16.32	0.35	1.28	0.49	0.63	0.43		
YFe_2Zn_{20}	31.35	0.68	2.86	0.46	1.32	0.88		
YRu_2Zn_{20}	18.72	0.41	1.0	0.3	0.3	0.67		
$GdCo_2Zn_{20}$	14.92						7.25	0.00
$GdFe_2Zn_{20}$	17.95						7.37	-0.84
$GdRu_2Zn_{20}$	17.15						7.34	-0.04

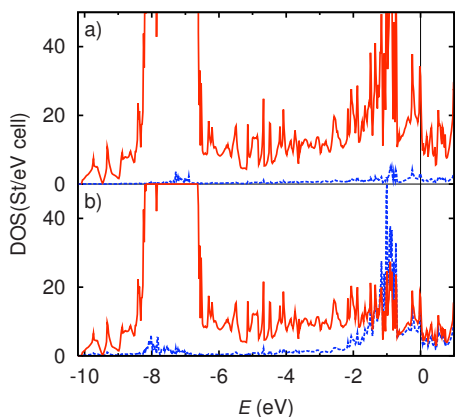


FIG. 18. (Color online) The DOS of YFe_2Zn_{20} (in St/eV cell) and partial DOS (in St/eV cell). E_F corresponds to zero energy. The red solid line in (a) corresponds to the total DOS and the blue dashed line to the PDOS of Y atoms. The red solid line in (b) corresponds to the PDOS of Zn and the blue dashed line to the PDOS of Fe atoms.

The negative coupling between Gd and transition metals induces magnetic moments on these atoms in a direction opposite to the Gd magnetic moment. In agreement with the high DOS of Fe atoms in YFe_2Zn_{20} , the induced magnetic moment on Fe atoms ($-0.84\mu_B$) is the largest among all examples. The smaller DOS of Ru atoms in YRu_2Zn_{20} correlates with a smaller induced magnetic moment on Ru in $GdRu_2Zn_{20}$ ($-0.04\mu_B$). The induced magnetic moment on Co is zero because of the compensation of interactions with Gd in AFM $GdCo_2Zn_{20}$. The calculated total magnetic moments, i.e., $7.25\mu_B$, $6.53\mu_B$, and $7.30\mu_B$, for GdT_2Zn_{20} ($T=Co, Fe,$ and Ru , respectively) are in good agreement with the experimental values of μ_{sat} , i.e., $7.3\mu_B$, $6.5\mu_B$, and $7.25\mu_B$ (see Table II). The DOS for $GdFe_2Zn_{20}$ [Fig. 20(a)] demonstrates a significant splitting between the occupied and empty 3d states of Fe, which is in agreement with sizable Fe magnetic

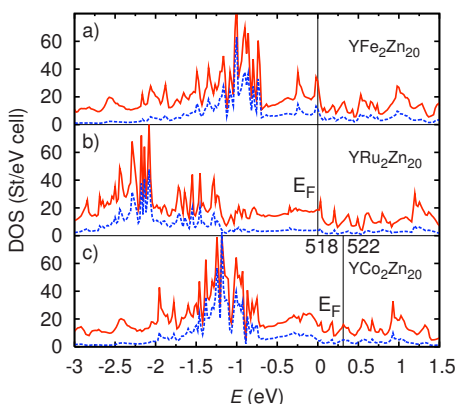


FIG. 19. (Color online) The DOS of (a) YFe_2Zn_{20} , (b) YRu_2Zn_{20} , and (c) YCo_2Zn_{20} near E_F (in St/eV cell) (solid line) and PDOS of Fe, Ru, and Co atoms (blue dashed line) (in St/eV cell). E_F is shown by vertical lines. 518 and 522 corresponds to the number of valence electrons in the unit cell calculated in the rigid band approximation from the DOS of YFe_2Zn_{20} .

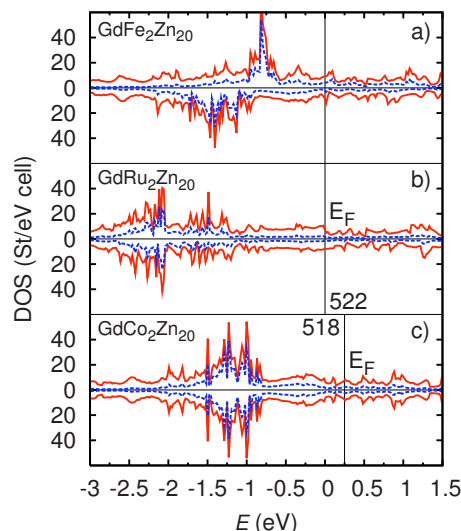


FIG. 20. (Color online) The red solid line corresponds to the DOS of (a) FM-ordered $GdFe_2Zn_{20}$, (b) FM-ordered $GdRu_2Zn_{20}$, and (c) AFM $GdCo_2Zn_{20}$ near E_F (in St/eV cell) and partial DOS of Fe, Ru, and Co atoms (blue dashed line) (in St/eV cell). E_F is shown by vertical lines. 518 and 522 corresponds to the number of valence electrons in the unit cell calculated in the rigid band approximation from the DOS.

moments, whereas this splitting is almost negligible in the case of Ru-based compounds [Fig. 20(b)].

E. $Gd(Fe_xCo_{1-x})_2Zn_{20}$ and $Y(Fe_xCo_{1-x})_2Zn_{20}$

Based on the distinct difference between the RFe_2Zn_{20} and RCo_2Zn_{20} compounds and motivated by the band structure calculations, a systematic study of $R(Fe_xCo_{1-x})_2Zn_{20}$ for $R=Gd$ and Y was carried out. In order to check x of $Gd(Fe_xCo_{1-x})_2Zn_{20}$ and $Y(Fe_xCo_{1-x})_2Zn_{20}$, energy dispersive spectra (EDS) measurement, a direct method for the determination of elemental concentrations, and powder x-ray diffraction measurement were employed. Figure 21 presents the EDS measurement results for the Gd series and the lattice constants for both series. The linear variation of lattice con-

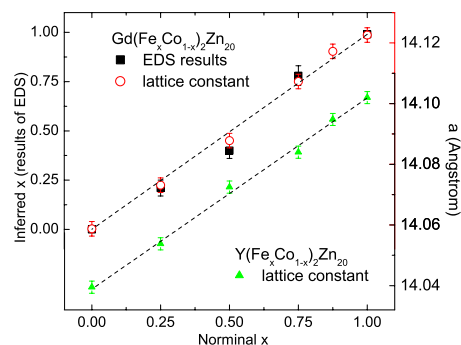


FIG. 21. (Color online) Lattice constants of the series of $Gd(Fe_xCo_{1-x})_2Zn_{20}$ (open circle) and $Y(Fe_xCo_{1-x})_2Zn_{20}$ (solid triangle). Fe concentration of $Gd(Fe_xCo_{1-x})_2Zn_{20}$ series inferred from EDS measurements (solid square).

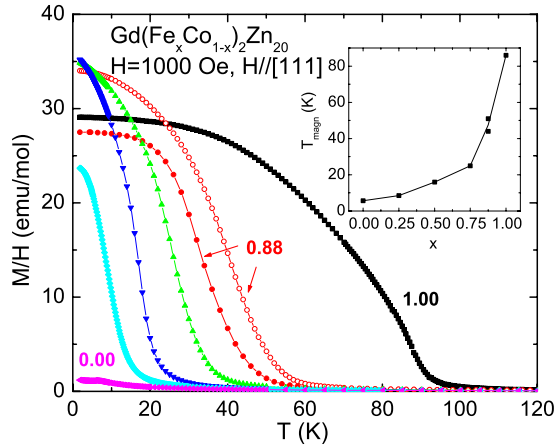


FIG. 22. (Color online) Zero field cooled M/H ($H=1000$ Oe) of $\text{Gd}(\text{Fe}_x\text{Co}_{1-x})_2\text{Zn}_{20}$ series versus temperature for $x=1.00, 0.88, 0.75, 0.50, 0.25,$ and 0 from right to left. Note that the data from two samples of $x=0.88$ are shown. Inset: Magnetic phase transition temperatures, obtained from the resistivity data, for $\text{Gd}(\text{Fe}_x\text{Co}_{1-x})_2\text{Zn}_{20}$.

starts with x for both series is compliant with Vegard's law, which is consistent with the results of EDS. Due to these results, the nominal x value is used from this point onward.

Figure 22 shows the magnetization divided by the applied field as a function of temperature for $\text{Gd}(\text{Fe}_x\text{Co}_{1-x})_2\text{Zn}_{20}$, which indicates FM ordering for $x > 0.25$. It should be noted that due to the zero-field-cooling process and the differing demagnetizing fields associated with the different sample shapes, the low-temperature magnetization in the FM state is not unique. As x is increased from 0 to 1, the polarizability of the electronic background [$\text{Y}(\text{Fe}_x\text{Co}_{1-x})_2\text{Zn}_{20}$] increases, and there is a monotonic but superlinear increase in T_{mag} (inset of Fig. 22), which is reminiscent of the x dependence of Z inferred from measurements on $\text{Y}(\text{Fe}_x\text{Co}_{1-x})_2\text{Zn}_{20}$.³ It is worth noting that the two samples with $x=0.88$ fall on this manifold, despite their slightly different T_C values. Placing Gd^{3+} ions into the matrix close to the Stoner limit seems to result in an enhanced sensitivity of small sample-to-sample variations. This sensitivity to the small disorder is not uncommon for the strongly correlated electronic system, particularly for the ones close to the Stoner criteria. For example, the different samples of ZrZn_2 , the canonical example of a weak ferromagnet, manifest a $\sim 10\%$ difference in their T_C 's.³⁷

The nature of the ordering for the whole series is further confirmed by the low-temperature magnetization isotherms (Fig. 23). For $x \geq 0.5$, the magnetization is representative of a FM-ordered state with a rapid rise and a saturation of the ordered moment in a field of the order of the estimated demagnetizing field, whereas the spin-flop transition near $H = 31$ kOe as well as the linear magnetization below it confirm a clear AFM-ordered state for $\text{GdCo}_2\text{Zn}_{20}$. For $x=0.25$, the magnetization is not a typical FM one: The saturation appears at ~ 10 kOe, which is much larger than the estimated maximum demagnetizing field. Such an anomaly may indicate the existence of frustration for $0 < x \leq 0.25$. The saturated moment extracted from the magnetization values under a 55 kOe applied field along the [111] crystallographic

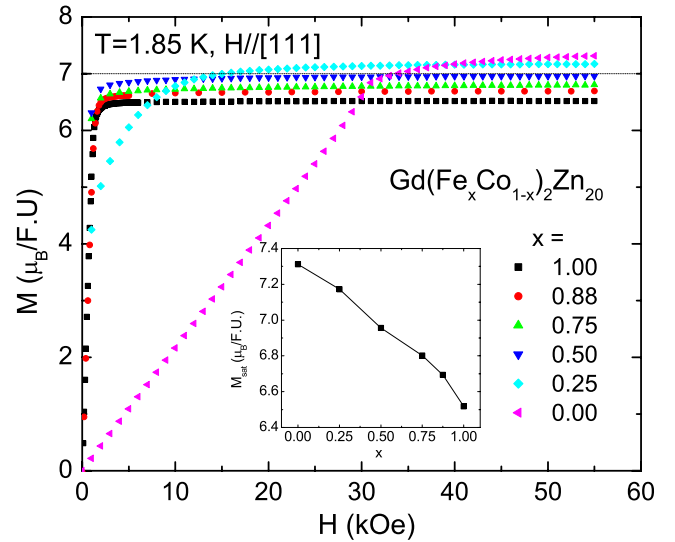


FIG. 23. (Color online) Low-temperature ($T=1.85$ K) magnetization versus applied field for the $\text{Gd}(\text{Fe}_x\text{Co}_{1-x})_2\text{Zn}_{20}$ series. Inset: Saturated moments as a function of x .

direction varies monotonically from the slightly enhanced value of $7.3\mu_B$ for $\text{GdCo}_2\text{Zn}_{20}$ to the slightly deficient value of $6.5\mu_B$ for $\text{GdFe}_2\text{Zn}_{20}$.³

IV. DISCUSSION

The band structure calculation indicates that with the same structure and similar lattice parameters, the diverse magnetic properties of $\text{GdT}_2\text{Zn}_{20}$ and $\text{YT}_2\text{Zn}_{20}$ are mainly dependent on the d -band conduction electrons from the transition metal site. The different d -band fillings of the Fe column members and the Co column members are associated with the different signs of the magnetic coupling of Gd^{3+} local moments and, therefore, the different types of magnetic ordering. Furthermore, the high and intermediately high $N(E_F)$ of $3d$ and $4d$ subbands of Fe and Ru, respectively, are associated with the strongly correlated electronic states of $\text{YFe}_2\text{Zn}_{20}$ and $\text{YRu}_2\text{Zn}_{20}$, as well as with the strong coupling between the Gd^{3+} local moments in $\text{GdFe}_2\text{Zn}_{20}$ and $\text{GdRu}_2\text{Zn}_{20}$ and, therefore, high magnetic ordering temperatures. The induced negative moment on the Fe site is not unexpected in intermetallic systems consisting of a heavy rare earth and a more than half-filled $3d$ transition metal,^{1,38} which can be understood in terms of the hybridization between the $3d$ electronic wave function of the transition metal and the $5d$ electronic wave function of the rare earth.³⁹

In addition to the electronic structure calculations, the remarkable high-temperature FM ordering of $\text{GdFe}_2\text{Zn}_{20}$ and $\text{GdRu}_2\text{Zn}_{20}$ can be understood in the conceptually simple context of large Heisenberg moments associated with the Gd^{3+} ion ($S=7/2$), which is embedded in the NFFL associated with $\text{YFe}_2\text{Zn}_{20}$ and $\text{YRu}_2\text{Zn}_{20}$. This framework has been employed to understand the anomalous high-temperature FM ordering in some systems of local moments in NFFL hosts, such as dilute Fe, Co, or Gd in Pd or Pt (Refs. 40 and 41) and RCO_2 ($R=\text{Gd}-\text{Tm}$).^{42,43} In these systems, the itinerant elec-

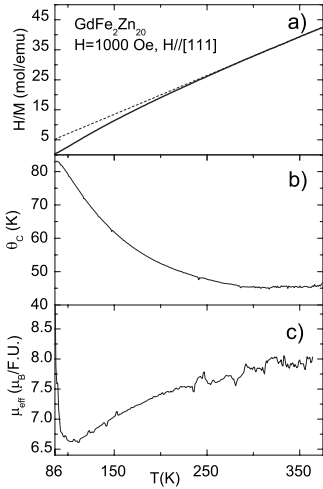


FIG. 24. (a) H/M ($H=1000$ kOe) of $\text{GdFe}_2\text{Zn}_{20}$ as a function of temperature. The dash line represents the Curie–Weiss fit above 250 K. (b) Temperature varied θ_c . (c) Temperature varied μ_{eff} . (See text.)

trons of the host (Pd, Pt, or YCo_2) are polarized by the local moments (Fe, Co, or R^{3+} ions), strongly couple them, and result in high-temperature local moment ordering and induced moment of the host.

The substitutional series of $\text{Gd}(\text{Fe}_x\text{Co}_{1-x})_2\text{Zn}_{20}$ and $\text{Y}(\text{Fe}_x\text{Co}_{1-x})_2\text{Zn}_{20}$ provides the versatility to study the correlation between the local moments and the highly polarizable host. When x is varied from 0 to 1, by tuning the d -band filling, the inferred values of Z for the $\text{Y}(\text{Fe}_x\text{Co}_{1-x})_2\text{Zn}_{20}$ series, representing to some extent the polarizability, increase superlinearly from 0.43 to 0.88,³ giving rise to the highly nonlinear increase of the magnetic ordering temperature for the $\text{Gd}(\text{Fe}_x\text{Co}_{1-x})_2\text{Zn}_{20}$ series (Fig. 22). This correspondence between the Z values and the magnetic ordering temperatures is even consistent with the T_C value for $\text{GdRu}_2\text{Zn}_{20}$, although the itinerant electrons of the transition metal are $4d$, not $3d$. Given $Z=0.67$ for $\text{YRu}_2\text{Zn}_{20}$, a similar Z value of the host is between $x=0.5$ and 0.75 for $\text{Y}(\text{Fe}_x\text{Co}_{1-x})_2\text{Zn}_{20}$.³ The T_C value for $\text{GdRu}_2\text{Zn}_{20}$ is also between the T_C values of $x=0.5$ and 0.75 for $\text{Gd}(\text{Fe}_x\text{Co}_{1-x})_2\text{Zn}_{20}$.

This conceptually simple framework can also help to understand the curious temperature dependence of the $1/\chi(T)$ data for $\text{GdFe}_2\text{Zn}_{20}$. Figure 24(a) shows the temperature dependent H/M in an applied field ($H=1000$ Oe), with a dashed line presenting the CW fit above 250 K. As shown before, the fit gives the value of the effective moment ($\mu_{\text{eff}}=7.9\mu_B$), which is comparable with the effective moment of the $4f$ electrons of Gd^{3+} in Hund’s ground state. The deviation from the CW law below 250 K has been explained as a result of temperature dependent coupling between Gd^{3+} local moments by means of a strongly polarizable electronic background.³ Assuming a constant μ_{eff} , one can extract the temperature dependence of θ_c from the $1/\chi$ data. As shown in Fig. 24(b), θ_c is essentially constant (~ 45 K) above 275 K and then increases monotonically as temperature decreases, tracking $\chi(T)$ of $\text{YFe}_2\text{Zn}_{20}$ (Fig. 15).

The correlation of the temperature dependent χ and the polarizability of the electronic background can also be seen

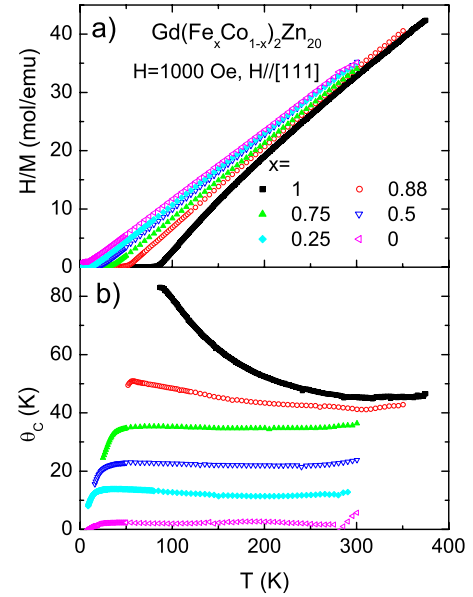


FIG. 25. (Color online) (a) H/M ($H=1000$ kOe) of $\text{Gd}(\text{Fe}_x\text{Co}_{1-x})_2\text{Zn}_{20}$ as a function of temperature. (b) Temperature varied θ_c . (See text.)

in the susceptibility of the $\text{Gd}(\text{Fe}_x\text{Co}_{1-x})_2\text{Zn}_{20}$ series. Figure 25(a) presents temperature dependent H/M under the applied field $H=1000$ Oe. Linear and parallel to each other at the high-temperature region, the data sets start to deviate at lower temperatures, especially for large x . As discussed before, the temperature dependent θ_c values were extracted with the assumption of an invariant μ_{eff} . Figure 25(b) shows that θ_c varies strongly, much weakly, and negligibly as $x=1, 0.88$, and ≤ 0.75 , respectively. For each x , the variation of θ_c tracks $\chi(T)$ of the $\text{Y}(\text{Fe}_x\text{Co}_{1-x})_2\text{Zn}_{20}$ series.³

An alternative method of analyzing the $\chi(T)$ data assumes that some induced moment exists above T_C and is aligned locally antiparallel to the Gd moment (in essence, forming a composite moment). Assuming an invariant θ_c , values of C can be inferred from the following:

$$\frac{1}{C} \approx \frac{d\left(\frac{T-\theta_c}{C}\right)}{dT} = \frac{d\left(\frac{H}{M}\right)}{dT}. \quad (3)$$

Figure 24(c) shows the monotonic decrease in μ_{eff} with a temperature decrease down to 110 K, at which it shows a minimum value of $6.6\mu_B$. From 100 K to T_C , μ_{eff} starts to increase in a highly nonlinear fashion. This increase in the μ_{eff} value is not unexpected in the vicinity of T_C in the FM system and could be due to the short range ordering or formation of magnetic clusters of the local moments.⁴⁴ The decrease in μ_{eff} in this scenario would be the result of the formation of magnetic droplets consisting of the Gd^{3+} local moments and the oppositely polarized electron cloud from the highly polarizable host. Such magnetic droplets are not unprecedented in analogous systems above T_C . For example, a “giant moment” was observed in a dilute Fe-Pd alloy⁴⁵; the deficient μ_{eff} of local moments was also found in the RCO_2 series ($R=\text{Gd-Tm}$) (Ref. 46) above T_C . Given that the pri-

mary difference between these two alternative explanations is in whether or not the itinerant electrons are polarized above T_C , measurements of Mössbauer spectra on the Fe sites at various temperatures can resolve this paradox.

V. SUMMARY

Six GdT_2Zn_{20} ($T=Fe, Ru, Os, Co, Rh,$ and Ir) compounds have magnetic properties that differ dramatically between the Fe column and Co column members. The Fe column members order ferromagnetically with the enhanced transition temperatures for the $T=Fe$ and Ru members, whereas the Co column members manifest low-temperature AFM ordering. In a related manner, the $T=Fe$ and Ru members of the YT_2Zn_{20} family manifest typical properties associated with NFFLs. Band structure calculation results for the $T=Fe$ and Ru members reveal that the large DOS at the Fermi level are correlated with the enhancement in their magnetic properties. The data on the pseudoternary series of compounds

$Gd(Fe_xCo_{1-x})_2Zn_{20}$ and $Y(Fe_xCo_{1-x})_2Zn_{20}$ further display the effect of different $3d$ -band filling on the magnetic properties of these two series. The conceptually simple framework of the Heisenberg moments embedded in the NFFL was discussed to understand the enhanced transitions for $GdFe_2Zn_{20}$ and $GdRu_2Zn_{20}$ and the curious temperature dependence of the $1/\chi$ versus T data for $GdFe_2Zn_{20}$.

ACKNOWLEDGMENTS

The authors thank J. Frederich for growing some of the compounds, L. Tan for Laue x-ray measurements, and E. D. Mun, X. Zong, J. Yan, R. W. McCallum, and R. Prozorov for helpful discussions. S.L.B. thanks David Lodge for valuable insights. Ames Laboratory is operated for the U.S. Department of Energy by Iowa State University under Contract No. DE-AC02-07CH11358. This work was supported by the Director for Energy Research, Office of Basic Energy Sciences.

- ¹J. J. M. Franse and R. J. Radwanski, in *Handbook of Magnetic Materials*, edited by K. H. J. Buschow (Elsevier, Amsterdam, 1993), Vol. 7, pp. 307–501.
- ²A. Szytula and J. Leciejewicz, *Handbook of Crystal Structures and Magnetic Properties of Rare Earth Intermetallics* (CRC, Boca Raton, 1994).
- ³S. Jia, S. L. Bud'ko, G. D. Samolyuk, and P. C. Canfield, *Nat. Phys.* **3**, 334 (2007).
- ⁴M. S. Torikachvili, S. Jia, E. D. Mun, S. T. Hannahs, R. C. Black, W. K. Neils, D. Martien, S. L. Bud'ko, and P. C. Canfield, *Proc. Natl. Acad. Sci. U.S.A.* **104**, 9960 (2007).
- ⁵S. Jia, N. Ni, S. L. Bud'ko, and P. C. Canfield, *Phys. Rev. B* **76**, 184410 (2007).
- ⁶T. Nasch, W. Jeitschko, and U. C. Rodewald, *Z. Naturforsch., B: Chem. Sci.* **52**, 1023 (1997).
- ⁷P. I. Kripyakevich and O. S. Zarechnyuk, *Dopov. Akad. Nauk Ukr. RSR, Ser. A: Fiz.-Tekh. Mat. Nauki* **30**, 364 (1968).
- ⁸V. M. T. Thiede, W. Jeitschko, S. Niemann, and T. Ebel, *J. Alloys Compd.* **267**, 23 (1998).
- ⁹O. Moze, L. D. Tung, J. J. M. Franse, and K. H. J. Buschow, *J. Alloys Compd.* **268**, 39 (1998).
- ¹⁰P. C. Canfield and Z. Fisk, *Philos. Mag. B* **65**, 1117 (1992).
- ¹¹X. Stoe, *AREA-Software Suite for the STOE IPDS II* (Stoe and Cie GmbH, Darmstadt, Germany, 2002).
- ¹²G. M. Sheldrick, *SHELXTL*, Bruker AXS, Inc., Madison, WI, USA, 2000.
- ¹³A. Eiling and J. S. Schilling, *J. Phys. F: Met. Phys.* **11**, 623 (1981).
- ¹⁴S. L. Bud'ko, R. H. T. Wilke, M. Angst, and P. C. Canfield, *Physica C* **420**, 83 (2005).
- ¹⁵S. Chikazumi and C. Graham, *Physics of Ferromagnetism* (Oxford University Press, New York, 1997).
- ¹⁶O. K. Andersen, *Phys. Rev. B* **12**, 3060 (1975).
- ¹⁷O. K. Andersen and O. Jepsen, *Phys. Rev. Lett.* **53**, 2571 (1984).
- ¹⁸U. von Barth and L. Hedin, *J. Phys. C* **5**, 1629 (1972).
- ¹⁹J. P. Perdew, K. Burke, and M. Ernzerhof, *Phys. Rev. Lett.* **77**, 3865 (1996).
- ²⁰A. Y. Perlov, S. V. Halilov, and H. Eschrig, *Phys. Rev. B* **61**, 4070 (2000).
- ²¹G. B. I. Turek, J. Kudrnovsky, and S. Blügel, *J. Phys.: Condens. Matter* **15**, 2771 (2003).
- ²²K. Schubert, *Kristallstrukturen zweikomponentiger Phasen* (Springer-Verlag, Berlin, 1964).
- ²³A. Arrott, *Phys. Rev.* **108**, 1394 (1957).
- ²⁴P. E. Brommer and J. J. M. Franse, in *Ferromagnetic Materials*, edited by K. H. J. Buschow and E. P. Wohlfarth (North-Holland, Amsterdam, 1990), Vol. 5, pp. 323–396.
- ²⁵I. Yeung, R. M. Roshko, and G. Williams, *Phys. Rev. B* **34**, 3456 (1986).
- ²⁶M. E. Fisher, *Philos. Mag.* **7**, 1731 (1962).
- ²⁷M. E. Fisher and J. S. Langer, *Phys. Rev. Lett.* **20**, 665 (1968).
- ²⁸J. M. Ziman, *Principles of the Theory of Solids* (Cambridge University Press, Cambridge, United Kingdom, 1979).
- ²⁹L. N. Mulay and E. A. Boudreaux, *Theory and Applications of Molecular Diamagnetism* (Wiley, New York, 1976).
- ³⁰ χ_0 and γ_0 values of Pd and Pt are extracted from G. S. Knapp and R. W. Jones, *Phys. Rev. B* **6**, 1761 (1972); B. Zeller, M. A. Paintner, and J. Voitländer, *J. Phys.: Condens. Matter* **16**, 919 (2004).
- ³¹ $\gamma_0=0.695$ mJ/mol K² [from C. Kittel, *Introduction to Solid State Physics* (Wiley, New York, 1986)], and $\chi_{0-dia}=13.4 \times 10^{-6}$ emu/mol (from Ref. 29).
- ³²N. W. Ashcroft and N. D. Mermin, *Solid State Physics* (Saunders, Philadelphia, 1976).
- ³³S. M. Hayden, G. G. Lonzarich, and H. L. Skriver, *Phys. Rev. B* **33**, 4977 (1986).
- ³⁴M. Shimizu, T. Takahashi, and A. Katsuki, *J. Phys. Soc. Jpn.* **18**, 240 (1963).
- ³⁵S. Tanaka and H. Harima, *J. Phys. Soc. Jpn.* **67**, 2594 (1998).
- ³⁶J. F. Janak, *Phys. Rev. B* **16**, 255 (1977).
- ³⁷See M. Seeger, H. Kronmüller, and H. J. Blythe, *J. Magn. Magn. Mater.* **139**, 312 (1995); C. Pfleiderer, M. Uhlarz, S. M. Hayden,

- R. Vollmer, H. v. Löhneysen, N. R. Bernhoeft, and G. G. Lonzarich, *Nature (London)* **412**, 58 (2001); E. A. Yelland, S. J. C. Yates, O. Taylor, A. Griffiths, S. M. Hayden, and A. Carrington, *Phys. Rev. B* **72**, 184436 (2005).
- ³⁸M. S. S. Brooks and B. Johansson, in *Handbook of Magnetic Materials*, edited by K. H. J. Buschow (Elsevier, Amsterdam, 1993), Vol. 7, pp. 139–230.
- ³⁹I. A. Campbell, *J. Phys. F: Met. Phys.* **2**, L47 (1972).
- ⁴⁰G. J. Nieuwenhuys, *Adv. Phys.* **24**, 515 (1975).
- ⁴¹J. Crangle, *Phys. Rev. Lett.* **13**, 569 (1964).
- ⁴²N. H. Duc and T. Goto, in *Handbook on the Physics and Chemistry of Rare Earths*, edited by K. A. Gschneidner, Jr. and L. Eyring (Elsevier, Amsterdam, 1999), Vol. 26, pp. 177–264.
- ⁴³N. H. Duc and P. E. Brommer, in *Handbook of Magnetic Materials*, edited by K. H. J. Buschow (Elsevier, Amsterdam, 1999), Vol. 12, pp. 259–394.
- ⁴⁴J. A. Mydosh, *Spin Glass: An Experimental Introduction* (Taylor & Francis, London, 1993).
- ⁴⁵A. M. Clogston, B. T. Matthias, M. Peter, H. J. Williams, E. Corenzwit, and R. C. Sherwood, *Phys. Rev.* **125**, 541 (1962).
- ⁴⁶A. M. Stewart, *J. Phys. C* **17**, 1557 (1984).